Entanglement purification and protection in a superconducting quantum network

Haoxiong Yan,[1,*] Youpeng Zhong,[1,†] Hung-Shen Chang,[1] Audrey Bienfait,[1,‡] Ming-Han Chou,[1,2] Christopher R. Conner,[1] Étienne Dumur,[1,3,§] Joel Grebel,[1] Rhys G. Povey,[1,2] and Andrew N. Cleland[1,3,¶]

[1]*Pritzker School of Molecular Engineering, University of Chicago, Chicago IL 60637, USA*

[2]*Department of Physics, University of Chicago, Chicago IL 60637, USA*

[3]*Center for Molecular Engineering and Material Science Division, Argonne National Laboratory, Lemont IL 60439, USA*

(Dated: January 13, 2022)

High-fidelity quantum entanglement is a key resource for quantum communication and distributed quantum computing, enabling quantum state teleportation, dense coding, and quantum encryption. Any sources of decoherence in the communication channel however degrade entanglement fidelity, thereby increasing the error rates of entangled state protocols. Entanglement purification provides a method to alleviate these non-idealities, by distilling impure states into higher-fidelity entangled states. Here we demonstrate the entanglement purification of Bell pairs shared between two remote superconducting quantum nodes connected by a moderately lossy, 1-meter long superconducting communication cable. We use a purification process to correct the dominant amplitude damping errors caused by transmission through the cable, with fractional increases in fidelity as large as 25%, achieved for higher damping errors. The best final fidelity the purification achieves is $94.09 \pm 0.98\%$. In addition, we use both dynamical decoupling and Rabi driving to protect the entangled states from local noise, increasing the effective qubit dephasing time by a factor of four, from 3 μs to 12 μs. These methods demonstrate the potential for the generation and preservation of very high-fidelity entanglement in a superconducting quantum communication network.

Superconducting qubits are a favored hardware platform for implementing quantum computation, with extant demonstrations of circuits with up to $\sim 10^2$ physical qubits [1–5]. However, there remain significant practical challenges in scaling up to the much larger qubit numbers needed for error correction and for the implementation of useful algorithms [6, 7]. Distributed quantum computing provides one path to scaling up, by connecting large numbers of small-scale quantum processors in a quantum network [8–11]. Initial steps have been taken to link small superconducting processors using superconducting transmission lines [12–20], as well as efforts to build coherent microwave-to-optical transducers for optical communication [21, 22]. However, other than monolithic demonstrations on a single chip [16], these have not realized the high fidelity entanglement needed for quantum information applications, with photon loss dominating the degradation of coherence during transmission through the cable interconnects, and decay due to local noise limiting the quantum state storage time.

Here we describe a superconducting quantum network with two physically-separated nodes, each including three superconducting qubits, connected by a 1-meter superconducting coaxial cable [19]. Using this setup, we can deterministically generate high-fidelity Bell pairs shared between the two nodes by sending microwave photons through the coaxial cable. Amplitude damping of the microwave photons however limits the fidelity of the entangled pairs. Here we demonstrate the use of an entanglement purification protocol [23] to correct these errors. Entanglement purification via distillation has been demonstrated in linear optics [24–27], as well as with trapped ions [28] and defects in diamond [29]. In superconducting qubits, mitigating the photon loss in a communication channel has been achieved using adiabatic methods [30] as well as through error-correctable

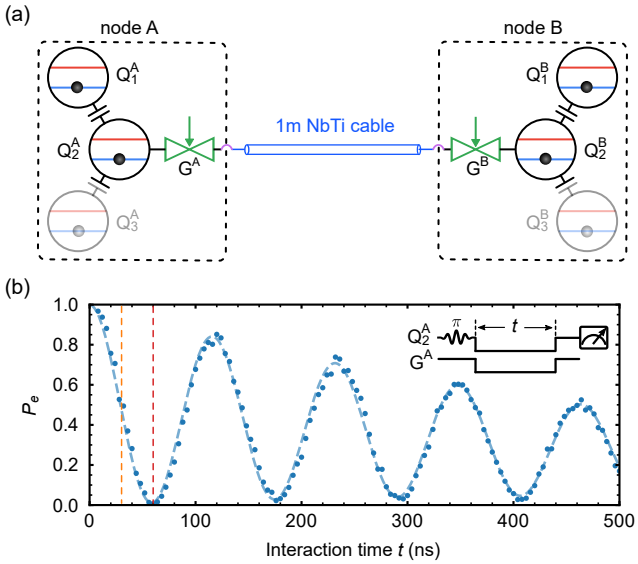

Figure 1. Device design and vacuum Rabi oscillations. (a) Schematic of the quantum network, comprising two nodes A and B, each with three capacitively-coupled xmon qubits $Q_i^{A,B}$ ($i = 1, 2, 3$). The center qubit $Q_2^{A,B}$ in each node is connected to a 1-meter long superconducting NbTi coaxial cable through a tunable coupler $G^{A,B}$. Qubits $Q_3^{A,B}$ are not used in this experiment. (b) Vacuum Rabi oscillations between Q_2^A and the 5.806 GHz communication mode C, measured with coupling strength set to $g^A/2\pi = 4.3$ MHz. Inset shows pulse sequence, where after exciting Q_2^A, the qubit is tuned into resonance with the communication mode while simultaneously turning on the coupler G^A. Blue dashed line is from numerical simulations. The orange and red dashed lines indicate the times for completing a half-swap and a full swap of the excitation in Q_2^A to the communication mode.

qubits [17]. In contrast to adiabatic protocols which require remote synchronization [30, 31], purification protocols can achieve near unit-fidelity Bell states using only local operations. The purification performance should be similar to protocols using error-correctable qubits, but with no additional requirements for intricate qubit encoding and quantum non-demolition measurements [17, 32]. Here we show that amplitude damping errors can be effectively corrected by a purification protocol including measurement and post-selection. In addition, we use dynamical decoupling (DD) and Rabi driving (RD) [33, 34] to protect the entangled states from local decoherence [35, 36], effectively increasing the qubit T_2 lifetime by a factor of four, from 3 μs to 12 μs. These results provide one possible route for the implementation of high-fidelity distributed quantum computing [8, 11, 37–39]. Please also see references in Ref. [40], which includes Refs. [41–44].

An overview of the experiment is shown in Fig. 1, with a schematic in Fig. 1(a), previously described in Ref. [19]. The system comprises two quantum network nodes A and B, where each node includes three capacitively-coupled superconducting qubits Q_i^k ($i = 1, 2, 3$; $k = A, B$), based on the xmon design [45, 46]. The central qubit Q_2^k in each node is directly coupled to a 1 m-long niobium-titanium (NbTi) superconducting coaxial cable via a tunable coupler G^k [47]. The tunable coupler is connected by superconducting aluminum wirebonds to the center and ground of the coaxial cable [19], effectively forming a Fabry-Pérot cavity with the tunable couplers serving as variable mirrors at either end. When the tunable couplers are turned to near zero coupling strength, the Fabry-Pérot modes have a free spectral range $\omega_{\rm FSR}/2\pi = 105$ MHz. Here we use the mode at 5.806 GHz mode for communication, with an energy lifetime of $T_{1r} = 477$ ns. The qubits each have a relaxation time of $T_1 \approx 10$ μs and dephasing time $T_2 \approx 3$ μs. Vacuum Rabi oscillations between Q_2^A and the communication mode C are shown

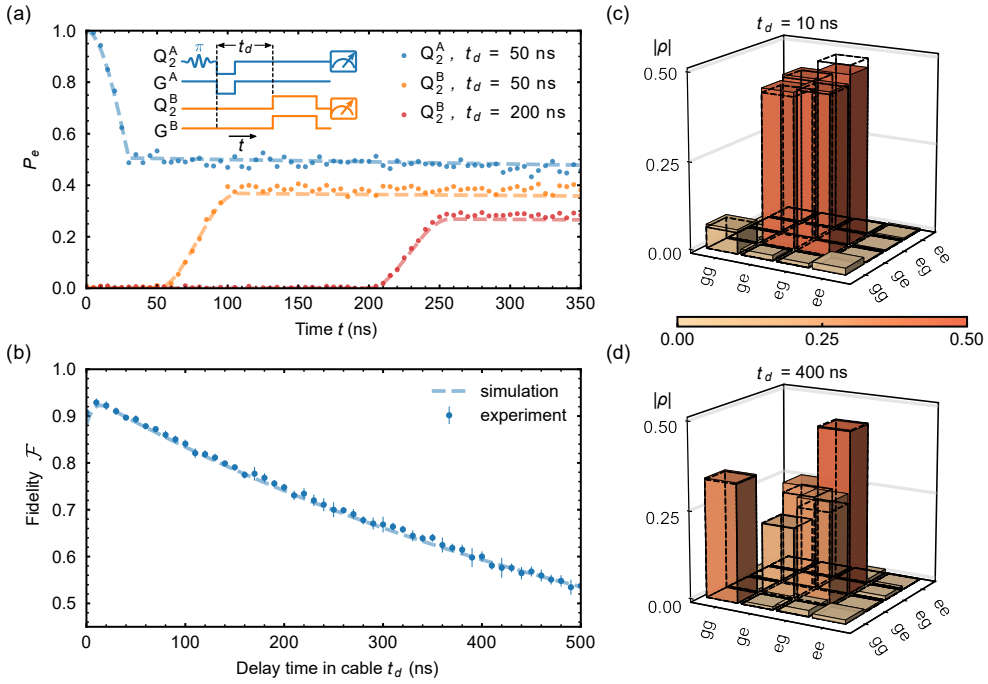

Figure 2. Deterministic Bell state generation. (a) Inset: Pulse sequence for Bell state generation, including the delay time $t_{\rm d}$ that the excitation resides in the communication mode C. Main plot shows $|e\rangle$ state population P_e in Q_2^A (blue), and in Q_2^B for different delay times in the cable $t_{\rm d} = 50$ ns (orange) and $t_{\rm d} = 200$ ns (red). (b) Bell state fidelity $\mathcal{F}$ as a function of delay time $t_{\rm d}$. (c) Bell state tomography for $t_{\rm d} = 10$ ns and (d) $t_{\rm d} = 400$ ns. Blue dashed lines in (b) and (b), and dashed outline boxes in (c) and (d), are results from numerical simulations.

in Fig. 1(b), where we excite Q_2^A, then turn on the coupler to coupling strength $g_A/2\pi = 4.3$ MHz while tuning the qubit into resonance with the communication mode; the other coupler is left off, effectively acting as a high-reflectance mirror. The qubit's excited state probability P_e is shown as a function of the interaction time t. More details can be found in Refs. [19, 40].

In Fig. 2 we display the deterministic generation of a Bell state distributed between nodes A and B. Using the tunable coupler, we swap a "half-photon" from Q_2^A to Q_2^B with the communication mode C as an intermediate bus. The pulse sequence is shown inset in Fig. 2(a), where we first apply a π pulse to bring Q_2^A from its ground state $|g\rangle$ to its first excited state $|e\rangle$, then turn on Q_2^A's coupler G^A to coupling strength $g^A/2\pi = 4.3$ MHz while tuning Q_2^A into resonance with the communication mode C. The swap time for a full photon emission ($|e0g\rangle \rightarrow i|g1g\rangle$, representing states as $|Q_2^A C Q_2^B\rangle$) is ~ 60 ns. Here we turn on the coupling for 30 ns, which swaps a half-excitation to the cable mode (ideally, $|e0g\rangle \rightarrow (|e0g\rangle + i|g1g\rangle)/\sqrt{2}$). We then turn off the coupler G^A, and after a time delay $t_{\rm d}$, set G^B's coupling strength to $g^B/2\pi = 4.3$ MHz while tuning Q_2^B into resonance with the communication mode. After a 60 ns full swap, this generates a Bell state between Q_2^A and Q_2^B, ideally $|\psi^-\rangle = (|eg\rangle - |ge\rangle)/\sqrt{2}$ (writing the two-qubit state as $|Q_2^A Q_2^B\rangle$). In Fig. 2(a) we show the excited state probability for Q_2^B for two different delay times, $t_{\rm d} = 50$ ns (orange) and 200 ns (red), along with Q_2^A (blue). These data clearly show the reduction in Q_2^B's excited state probability P_e with delay time $t_{\rm d}$.

In Fig. 2(b) we display the effect of the delay time in the cable $t_{\rm d}$ on the Bell state fidelity $\mathcal{F}$, defined as $\mathcal{F} = \langle\psi^-|\rho|\psi^-\rangle$, displaying the two-qubit density matrix ρ measured using state tomography [48]. Numerical simulations (dashed blue line; see [40]) are in good agreement with the measurements. In Fig. 2(c-d) we show the measured density matrices for the time delays

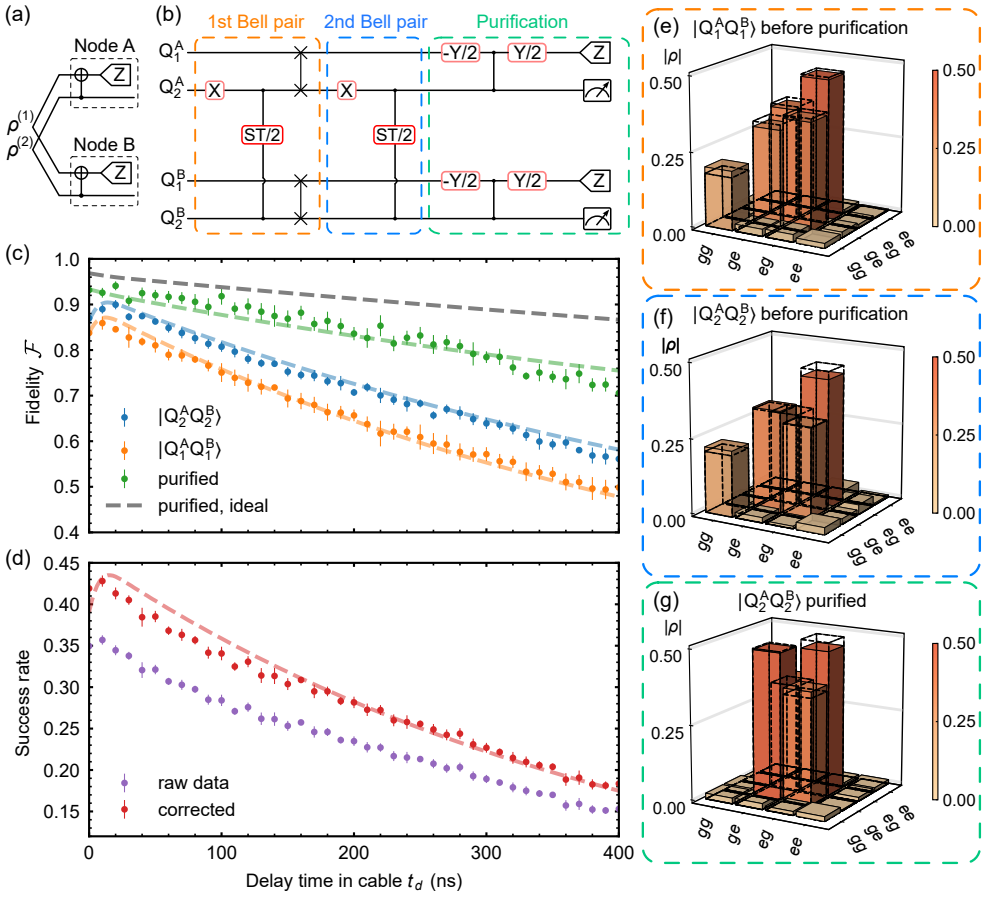

Figure 3. Entanglement purification. (a) Circuit schematic. (b) Experimental realization of the purification circuit in (a). The ST/2 process is a "half-photon" transfer process as in Fig. 2(a). We prepare the first Bell pair $|Q_2^AQ_2^B\rangle$ followed by swaps into $|Q_1^AQ_1^B\rangle$. We then generate the second Bell pair in $|Q_2^AQ_2^B\rangle$, and purify using these two pairs. (c) Bell state fidelity $\mathcal{F}$ before purification for $|Q_2^AQ_2^B\rangle$ (blue) and $|Q_1^AQ_1^B\rangle$ (orange), and after purification for $|Q_2^AQ_2^B\rangle$ (green), each measured as a function of delay time $t_{\rm d}$. Grey dashed line is for error-free purification between two identical impure Bell states. (d) Success rate for purification, which is the probability of measuring $|Q_1^AQ_1^B\rangle\rangle$ in $|ee\rangle$ with (red) and without (purple) readout measurement correction [49]. (e) State tomography with $t_{\rm d} = 150$ ns for the pre-purification states $|Q_1^AQ_1^B\rangle$, representing $\rho^{(1)}$, with state fidelity $69.4 \pm 2.0\%$, and for (f) $|Q_2^AQ_2^B\rangle$, representing $\rho^{(2)}$, with state fidelity $75.3 \pm 1.0\%$. (g) Tomography for the post-purified $|Q_2^AQ_2^A\rangle$, representing $\rho_{\rm f}$, with state fidelity $86.9 \pm 1.8\%$. Dashed lines are simulation results.

$t_{\rm d} = 10$ ns and $t_{\rm d} = 400$ ns. For the data in Fig. 2(c), the measured fidelity to the ideal Bell state is $\mathcal{F} = 92.89 \pm 0.85\%$, close to the numerical simulation result $\mathcal{F}^{\rm sim} = 92.01\%$. The data indicate that the dominant infidelity is due to damping errors ($|1\rangle \rightarrow |0\rangle$) in the cable, which increase with delay time in the cable, with a much smaller contribution from phase errors in the qubits $(|g\rangle + |e\rangle)/\sqrt{2} \leftrightarrow (|g\rangle - |e\rangle)/\sqrt{2}$. Damping results in a larger $|{\rm Tr}(\rho|gg\rangle\langle gg|)|$ component in the density matrix, while phase decoherence yields smaller off-diagonal terms in ρ. From the data at delay $t_{\rm d} = 400$ ns, we estimate that $\sim 94\%$ percent of the infidelity is due to damping errors ($\sim 82\%$ from cable loss and $\sim 12\%$ from qubit decay) and $\sim 6\%$ percent is due to qubit decoherence.

We use a purification process including measurement and post-selection to improve the final Bell state fidelities, as shown in Fig. 3. The purification circuit is shown in Fig. 3(a), where two impure Bell pairs $\rho^{(1)}$ and $\rho^{(2)}$ are created between the two

nodes, which serve as the source ($\rho^{(1)}$) and target pairs ($\rho^{(2)}$). Parallel CNOT gates are performed between the qubits in each node, followed by Z measurements of the source pair $\rho^{(1)}$, using the measurement results to post-select from $\rho^{(2)}$. The result is a purified Bell pair $\rho_{\rm f}$ with a higher fidelity to the purification target state $|\psi^+\rangle = (|eg\rangle + |ge\rangle)/\sqrt{2}$ [23].

Including only the errors due to the lossy channel and qubit dephasing, the two nominally-identical impure states can be written as

$$\begin{aligned}\rho^{(1)} = \rho^{(2)} = (1-\epsilon_p)|\psi^-\rangle\langle\psi^-| + \epsilon_p|\psi^+\rangle\langle\psi^+| \\ +\epsilon_d(|gg\rangle\langle gg| - |ge\rangle\langle ge|)\end{aligned} \tag{1}$$

where ϵ_d accounts for any damping errors in the cable, of the form $|1\rangle \rightarrow |0\rangle$, and ϵ_p accounts for phase errors of the form $(|g\rangle + |e\rangle)/\sqrt{2} \leftrightarrow (|g\rangle - |e\rangle)/\sqrt{2}$, which take $|\psi^-\rangle$ to $|\psi^+\rangle = (|eg\rangle + |ge\rangle)/\sqrt{2}$.

When the two Z measurements of $\rho^{(1)}$ are not consistent, the state $\rho_{\rm f}$ will be a mixed state, indicating a failed purification. Assuming perfect local operations and measurements, when the two measurement results are consistent, the result is a purified state closer to the ideal $|\psi^+\rangle$ pair. When the measurement result of $\rho^{(1)}$ is $|gg\rangle$, damping errors are partially corrected, with a non-zero ground state $|gg\rangle\langle gg|$ population. For more details see [40].

When instead the measurement result is $|ee\rangle$, the final state will be

$$\rho_{\rm f} = (1-\epsilon_{p_f})|\psi^+\rangle\langle\psi^+| + \epsilon_{p_f}|\psi^-\rangle\langle\psi^-|, \tag{2}$$

with a phase error $\epsilon_{p_f} = (2\epsilon_p^2 - 2\epsilon_p + 2\epsilon_d)/(1-2\epsilon_d)$ [40]. The damping error is fully corrected, with a purification success rate $0.5 - \epsilon_d$. Here we focus on the measurement result $|ee\rangle$, where the damping error is fully corrected and purification yields higher Bell state fidelities than the $|gg\rangle$ measurement result.

We implement the purification process as shown in Fig. 3(b). After generating the first Bell pair, shared between the two nodes in $|Q_2^A Q_2^B\rangle$, we apply two parallel iSWAP gates that transfer the state to $|Q_1^A Q_1^B\rangle$, with an efficiency over 99%. We then generate the second Bell pair in $|Q_2^A Q_2^B\rangle$ using the same sequence as for the the first Bell pair. We indirectly vary the cable loss by changing the delay time $t_{\rm d}$ the half-photon resides in the cable.

Pre-purification measurements of the two Bell states in $|Q_1^A Q_1^B\rangle$ and $|Q_2^A Q_2^B\rangle$, representing $\rho^{(1)}$ and $\rho^{(2)}$ respectively, are shown in Fig. 3(c), (e) and (f). These indicate the fidelity of the second Bell pair in $|Q_2^A Q_2^B\rangle$ is a few percent lower than the Bell pair in Fig. 2(b), due to imperfections in the iSWAP gates and possible interference with the first Bell pair during the second Bell pair generation. The first Bell pair's fidelity also falls due to qubit decay during the second Bell pair generation. Better qubit lifetimes [50, 51], or the use of parallel communication channels, could reduce these infidelities. The purifying CNOT gate, with $|Q_2^A Q_2^B\rangle$ as the control, is implemented using a CZ gate combined with two single-qubit $Y/2$ gates applied to $|Q_1^A Q_1^B\rangle$. The CZ gate is realized using the qubits' second excited state $|f\rangle$, bringing the two-qubit states $|ee\rangle$ and $|gf\rangle$ into energy resonance so that the $|ee\rangle$ state acquires an extra phase compared to the other computational basis states [52]. We typically achieve CZ gate process fidelities of over 95% [40]. Following the CNOT gates, we perform Z measurements of $Q_1^{A,B}$ and tomography measurements of $Q_2^{A,B}$. We post-select as purified states those with $|Q_1^A Q_1^B\rangle = |ee\rangle$; this purification process targets the ideal Bell state $|\psi^+\rangle$.

The fidelity of the purified state, representing $\rho_{\rm f}$, is shown in Fig. 3(c) as a function of delay $t_{\rm d}$. Larger $t_{\rm d}$ shows larger purification improvement, as there is more photon loss during cable transmission; the best fidelity of $94.09\% \pm 0.98\%$ is for the shortest delay $t_{\rm d} = 20$ ns. The largest fractional improvement in fidelity, defined as the change in fidelity divided by the

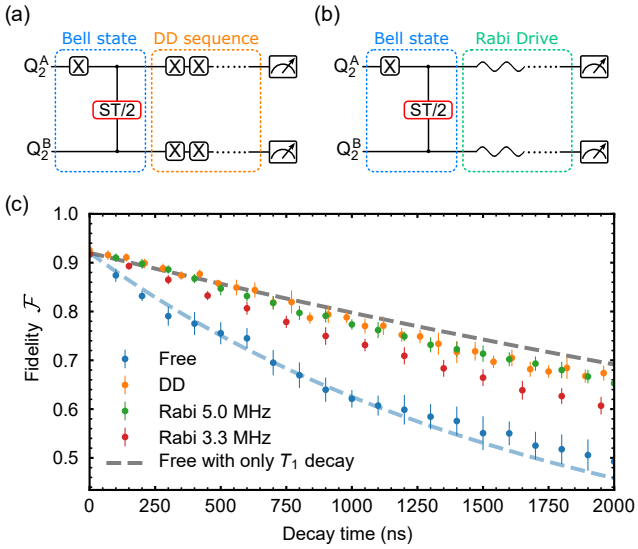

Figure 4. Entanglement protection using either dynamical decoupling (DD) or Rabi driving. (a) Pulse sequence for DD and (b) Rabi drive. The $\mathrm{ST}/2$ gate corresponds to the half-photon transfer process as shown in Fig. 2(b), with cable delay $t_\mathrm{d} = 10$ ns. (c) Bell state fidelity as a function of time for free evolution (blue), DD (orange), and for Rabi drive strengths $\Omega/2\pi = 5$ MHz (green) and $\Omega/2\pi = 3.3$ MHz (red). Numerical simulations are for free evolution including amplitude and phase decay (blue dashed line) and for free evolution with only T_1 decay (grey dashed line).

initial (pre-purification) fidelity, is 25%, achieved for the longest delay $t_\mathrm{d} = 400$ ns. The success rate, given by the probability of measuring $|Q_1^A Q_1^B\rangle$ in $|ee\rangle$, is shown in Fig. 3(d), which falls for longer delay times, as expected: The main limitation is due to storage decay of the first Bell pair, whose resultingly lower fidelity limits both the success rate and the purified fidelity. The gray dashed line shows the expected purified Bell state fidelity for two identical Bell pairs matching $|Q_2^A Q_2^B\rangle$. State tomography of the purified state for $t_\mathrm{d} = 150$ ns is shown in Fig. 4(g), with a state fidelity $86.9 \pm 1.8\%$. The purified state has more than 10% fidelity improvement and damping errors are mostly corrected.

The purification protocol is mostly limited by decoherence in the qubits. The dephasing time $T_2 \sim 3$ μs of our qubits is significantly shorter than the energy relaxation time $T_1 \sim 10$ μs, indicative of extra dephasing channels, possibly due to magnetic flux noise, to which frequency-tunable xmons are particularly susceptible [45]. Using either dynamical decoupling (DD), or a simpler Rabi drive (RD), we can protect the Bell pairs from the local noise that generates some of this decoherence. DD is a technique commonly used in spin systems [33, 34], where periodic pulse sequences average the effective environmental noise to near zero, yielding significantly extended qubit coherence times [35, 36, 53], as well as suppression of two-qubit correlated noise [54]. The quantum circuit for DD is shown in Fig. 4(a), where we apply a sequence of X gates to both qubits after generating a Bell state; the simpler RD is shown in Fig. 4(b). The DD X gate we use is a π-pulse with an additional DRAG correction [55]. The gate fidelity, as determined by randomized benchmarking [56], is 99.7%, with a gate duration of 30 ns [40]. Following each X gate, we insert 5 ns of buffer time, so that each DD cycle, comprising two X gates, takes 70 ns. To evaluate the performance of the DD sequence, we perform state tomography after a varying number of DD cycles, with the results shown in Fig. 4(d). We see that DD significantly improves the Bell state fidelity, approaching the fidelity associated with pure T_1 dephasing (gray dashed line). For a 1.4 μs evolution time, the state fidelity improves from $57.6 \pm 3.0\%$ to $71.7 \pm 2.3\%$.

The simpler Rabi drive scheme works nearly as well as DD. The fidelity of the Bell pair with Rabi drive is shown in Fig. 4(d), showing similar performance to the DD sequence for $\Omega/2\pi = 5$ MHz. For 1.4 μs evolution, the RD fidelity improves from $57.6 \pm 3.0\%$ to $72.3 \pm 1.5\%$. For both DD and RD, the Bell state fidelity decay corresponds well to simulations using a qubit $T_2 \sim 12$ μs, showing excellent protection of entanglement from local noise. We also tried to combine RD/DD with the purification protocol to further improve the performance. However this was not successful, we believe because of interference with the frequency-bias pulses applied to $|Q_1^A Q_1^B\rangle$ [40].

In conclusion, we have demonstrated a two-node superconducting quantum network that supports the high-fidelity generation of Bell pairs across the network, with excellent state fidelity of $92.89 \pm 0.85\%$. Purification protocols successfully correct amplitude damping errors caused by the lossy communication channel, improving the state fidelity to $94.09 \pm 0.98\%$. Furthermore, local phase decoherence can be minimized using either dynamical decoupling or the simpler Rabi drive. These results point to the powerful potential for distributed quantum computing in superconducting networks, relying on high-fidelity entanglement over meter-scale networks.

ACKNOWLEDGEMENTS

We thank Liang Jiang, David Schuster and Peter Duda for helpful discussions, and W. D. Oliver and G. Calusine at MIT Lincoln Lab for providing the traveling-wave parametric amplifier (TWPA) used in this work. Devices and experiments were supported by the Air Force Office of Scientific Research and the Army Research Laboratory. É.D. was supported by LDRD funds from Argonne National Laboratory; A.N.C. was supported in part by the DOE, Office of Basic Energy Sciences. This work was partially supported by UChicago's MRSEC (NSF award DMR-2011854) and by the NSF QLCI for HQAN (NSF Award 2016136). We made use of the Pritzker Nanofabrication Facility, which receives support from SHyNE, a node of the National Science Foundation's National Nanotechnology Coordinated Infrastructure (NSF Grant No. NNCI ECCS-2025633). The authors declare no competing financial interests. Correspondence and requests for materials should be addressed to A. N. Cleland (anc@uchicago.edu).

---

* These two authors contributed equally

† These two authors contributed equally; Present Address: Shenzhen Institute for Quantum Science and Engineering, Southern University of Science and Technology, Shenzhen 518055, China

‡ Present Address: Université de Lyon, ENS de Lyon, Université Claude Bernard, CNRS, Laboratoire de Physique, F-69342 Lyon, France

§ Present Address: Université Grenoble Alpes, CEA, INAC-Pheliqs, 38000 Grenoble, France

¶ anc@uchicago.edu

[1] R. Barends, J. Kelly, A. Megrant, A. Veitia, D. Sank, E. Jeffrey, T. C. White, J. Mutus, A. G. Fowler, B. Campbell, Y. Chen, Z. Chen, B. Chiaro, A. Dunsworth, C. Neill, P. O'Malley, P. Roushan, A. Vainsencher, J. Wenner, A. N. Korotkov, A. N. Cleland, and J. M. Martinis, Superconducting quantum circuits at the surface code threshold for fault tolerance, Nature **508**, 500 (2014).

[2] F. Arute, K. Arya, R. Babbush, D. Bacon, J. C. Bardin, R. Barends, R. Biswas, S. Boixo, F. G. S. L. Brandao, D. A. Buell, B. Burkett, Y. Chen, Z. Chen, B. Chiaro, R. Collins, W. Courtney, A. Dunsworth, E. Farhi, B. Foxen, A. Fowler, C. Gidney, M. Giustina, R. Graff, K. Guerin, S. Habegger, M. P. Harrigan, M. J. Hartmann, A. Ho, M. Hoffmann, T. Huang, T. S. Humble, S. V. Isakov, E. Jeffrey, Z. Jiang, D. Kafri, K. Kechedzhi, J. Kelly, P. V. Klimov, S. Knysh, A. Korotkov, F. Kostritsa, D. Landhuis, M. Lindmark, E. Lucero, D. Lyakh,

S. Mandrà, J. R. McClean, M. McEwen, A. Megrant, X. Mi, K. Michielsen, M. Mohseni, J. Mutus, O. Naaman, M. Neeley, C. Neill, M. Y. Niu, E. Ostby, A. Petukhov, J. C. Platt, C. Quintana, E. G. Rieffel, P. Roushan, N. C. Rubin, D. Sank, K. J. Satzinger, V. Smelyanskiy, K. J. Sung, M. D. Trevithick, A. Vainsencher, B. Villalonga, T. White, Z. J. Yao, P. Yeh, A. Zalcman, H. Neven, and J. M. Martinis, Quantum supremacy using a programmable superconducting processor, Nature **574**, 505 (2019).

[3] P. Jurcevic, A. Javadi-Abhari, L. S. Bishop, I. Lauer, D. F. Bogorin, M. Brink, L. Capelluto, O. Günlük, T. Itoko, N. Kanazawa, A. Kandala, G. A. Keefe, K. Krsulich, W. Landers, E. P. Lewandowski, D. T. McClure, G. Nannicini, A. Narasgond, H. M. Nayfeh, E. Pritchett, M. B. Rothwell, S. Srinivasan, N. Sundaresan, C. Wang, K. X. Wei, C. J. Wood, J.-B. Yau, E. J. Zhang, O. E. Dial, J. M. Chow, and J. M. Gambetta, Demonstration of quantum volume 64 on a superconducting quantum computing system, Quantum Science and Technology **6**, 025020 (2021).

[4] M. Gong, S. Wang, C. Zha, M.-C. Chen, H.-L. Huang, Y. Wu, Q. Zhu, Y. Zhao, S. Li, S. Guo, H. Qian, Y. Ye, F. Chen, C. Ying, J. Yu, D. Fan, D. Wu, H. Su, H. Deng, H. Rong, K. Zhang, S. Cao, J. Lin, Y. Xu, L. Sun, C. Guo, N. Li, F. Liang, V. M. Bastidas, K. Nemoto, W. J. Munro, Y.-H. Huo, C.-Y. Lu, C.-Z. Peng, X. Zhu, and J.-W. Pan, Quantum walks on a programmable two-dimensional 62-qubit superconducting processor, Science **372**, 948 (2021).

[5] Y. Wu, W.-S. Bao, S. Cao, F. Chen, M.-C. Chen, X. Chen, T.-H. Chung, H. Deng, Y. Du, D. Fan, M. Gong, C. Guo, C. Guo, S. Guo, L. Han, L. Hong, H.-L. Huang, Y.-H. Huo, L. Li, N. Li, S. Li, Y. Li, F. Liang, C. Lin, J. Lin, H. Qian, D. Qiao, H. Rong, H. Su, L. Sun, L. Wang, S. Wang, D. Wu, Y. Xu, K. Yan, W. Yang, Y. Yang, Y. Ye, J. Yin, C. Ying, J. Yu, C. Zha, C. Zhang, H. Zhang, K. Zhang, Y. Zhang, H. Zhao, Y. Zhao, L. Zhou, Q. Zhu, C.-Y. Lu, C.-Z. Peng, X. Zhu, and J.-W. Pan, Strong quantum computational advantage using a superconducting quantum processor, Physical Review Letters **127**, 180501 (2021).

[6] A. G. Fowler, M. Mariantoni, J. M. Martinis, and A. N. Cleland, Surface codes: Towards practical large-scale quantum computation, Physical Review A **86**, 032324 (2012).

[7] J. B. Hertzberg, E. J. Zhang, S. Rosenblatt, E. Magesan, J. A. Smolin, J.-B. Yau, V. P. Adiga, M. Sandberg, M. Brink, J. M. Chow, and J. S. Orcutt, Laser-annealing josephson junctions for yielding scaled-up superconducting quantum processors, npj Quantum Information **7**, 129 (2021).

[8] D. Gottesman and I. L. Chuang, Demonstrating the viability of universal quantum computation using teleportation and single-qubit operations, Nature **402**, 390 (1999).

[9] L. Jiang, J. M. Taylor, A. S. Sørensen, and M. D. Lukin, Distributed quantum computation based on small quantum registers, Physical Review A **76**, 062323 (2007).

[10] H. J. Kimble, The quantum internet, Nature **453**, 1023 (2008).

[11] C. Monroe, R. Raussendorf, A. Ruthven, K. R. Brown, P. Maunz, L.-M. Duan, and J. Kim, Large-scale modular quantum-computer architecture with atomic memory and photonic interconnects, Physical Review A **89**, 022317 (2014).

[12] P. Kurpiers, P. Magnard, T. Walter, B. Royer, M. Pechal, J. Heinsoo, Y. Salathé, A. Akin, S. Storz, J.-C. Besse, S. Gasparinetti, A. Blais, and A. Wallraff, Deterministic quantum state transfer and remote entanglement using microwave photons, Nature **558**, 264 (2018).

[13] C. J. Axline, L. D. Burkhart, W. Pfaff, M. Zhang, K. Chou, P. Campagne-Ibarcq, P. Reinhold, L. Frunzio, S. M. Girvin, L. Jiang, M. H. Devoret, and R. J. Schoelkopf, On-demand quantum state transfer and entanglement between remote microwave cavity memories, Nature Physics **14**, 705 (2018).

[14] P. Campagne-Ibarcq, E. Zalys-Geller, A. Narla, S. Shankar, P. Reinhold, L. Burkhart, C. Axline, W. Pfaff, L. Frunzio, R. Schoelkopf, and M. Devoret, Deterministic remote entanglement of superconducting circuits through microwave two-photon transitions, Physical Review Letters **120**, 200501 (2018).

[15] N. Leung, Y. Lu, S. Chakram, R. K. Naik, N. Earnest, R. Ma, K. Jacobs, A. N. Cleland, and D. I. Schuster, Deterministic bidirectional communication and remote entanglement generation between superconducting qubits, npj Quantum Information **5**, 18 (2019).

[16] Y. P. Zhong, H.-S. Chang, K. J. Satzinger, M.-H. Chou, A. Bienfait, C. R. Conner, É. Dumur, J. Grebel, G. A. Peairs, R. G. Povey, D. I. Schuster, and A. N. Cleland, Violating bell's inequality with remotely connected superconducting qubits, Nature Physics **15**, 741 (2019).

[17] L. D. Burkhart, J. D. Teoh, Y. Zhang, C. J. Axline, L. Frunzio, M. Devoret, L. Jiang, S. Girvin, and R. Schoelkopf, Error-detected state

transfer and entanglement in a superconducting quantum network, PRX Quantum **2**, 030321 (2021).

[18] P. Magnard, S. Storz, P. Kurpiers, J. Schär, F. Marxer, J. Lütolf, T. Walter, J.-C. Besse, M. Gabureac, K. Reuer, A. Akin, B. Royer, A. Blais, and A. Wallraff, Microwave quantum link between superconducting circuits housed in spatially separated cryogenic systems, Physical Review Letters **125**, 260502 (2020).

[19] Y. Zhong, H.-S. Chang, A. Bienfait, É. Dumur, M.-H. Chou, C. R. Conner, J. Grebel, R. G. Povey, H. Yan, D. I. Schuster, and A. N. Cleland, Deterministic multi-qubit entanglement in a quantum network, Nature **590**, 571 (2021).

[20] A. Gold, J. P. Paquette, A. Stockklauser, M. J. Reagor, M. S. Alam, A. Bestwick, N. Didier, A. Nersisyan, F. Oruc, A. Razavi, B. Scharmann, E. A. Sete, B. Sur, D. Venturelli, C. J. Winkleblack, F. Wudarski, M. Harburn, and C. Rigetti, Entanglement across separate silicon dies in a modular superconducting qubit device, npj Quantum Information **7**, 142 (2021).

[21] X. Han, W. Fu, C. Zhong, C.-L. Zou, Y. Xu, A. A. Sayem, M. Xu, S. Wang, R. Cheng, L. Jiang, and H. X. Tang, Cavity piezo-mechanics for superconducting-nanophotonic quantum interface, Nature Communications **11**, 3237 (2020).

[22] M. Mirhosseini, A. Sipahigil, M. Kalaee, and O. Painter, Superconducting qubit to optical photon transduction, Nature **588**, 599 (2020).

[23] C. H. Bennett, G. Brassard, S. Popescu, B. Schumacher, J. A. Smolin, and W. K. Wootters, Purification of noisy entanglement and faithful teleportation via noisy channels, Physical Review Letters **76**, 722 (1996).

[24] J.-W. Pan, C. Simon, Č. Brukner, and A. Zeilinger, Entanglement purification for quantum communication, Nature **410**, 1067 (2001).

[25] J.-W. Pan, S. Gasparoni, R. Ursin, G. Weihs, and A. Zeilinger, Experimental entanglement purification of arbitrary unknown states, Nature **423**, 417 (2003).

[26] X.-M. Hu, C.-X. Huang, Y.-B. Sheng, L. Zhou, B.-H. Liu, Y. Guo, C. Zhang, W.-B. Xing, Y.-F. Huang, C.-F. Li, and G.-C. Guo, Long-distance entanglement purification for quantum communication, Physical Review Letters **126**, 010503 (2021).

[27] S. Ecker, P. Sohr, L. Bulla, M. Huber, M. Bohmann, and R. Ursin, Experimental single-copy entanglement distillation, Physical Review Letters **127**, 040506 (2021).

[28] R. Reichle, D. Leibfried, E. Knill, J. Britton, R. B. Blakestad, J. D. Jost, C. Langer, R. Ozeri, S. Seidelin, and D. J. Wineland, Experimental purification of two-atom entanglement, Nature **443**, 838 (2006).

[29] N. Kalb, A. A. Reiserer, P. C. Humphreys, J. J. W. Bakermans, S. J. Kamerling, N. H. Nickerson, S. C. Benjamin, D. J. Twitchen, M. Markham, and R. Hanson, Entanglement distillation between solid-state quantum network nodes, Science **356**, 928 (2017).

[30] H.-S. Chang, Y. Zhong, A. Bienfait, M.-H. Chou, C. Conner, É. Dumur, J. Grebel, G. Peairs, R. Povey, K. Satzinger, and A. Cleland, Remote entanglement via adiabatic passage using a tunably dissipative quantum communication system, Physical Review Letters **124**, 240502 (2020).

[31] N. V. Vitanov, A. A. Rangelov, B. W. Shore, and K. Bergmann, Stimulated raman adiabatic passage in physics, chemistry, and beyond, Reviews of Modern Physics **89**, 015006 (2017).

[32] W. Dür and H. J. Briegel, Entanglement purification and quantum error correction, Reports on Progress in Physics **70**, 1381 (2007).

[33] H. Y. Carr and E. M. Purcell, Effects of diffusion on free precession in nuclear magnetic resonance experiments, Physical Review **94**, 630 (1954).

[34] S. Meiboom and D. Gill, Modified spin-echo method for measuring nuclear relaxation times, Review of Scientific Instruments **29**, 688 (1958).

[35] J. Bylander, S. Gustavsson, F. Yan, F. Yoshihara, K. Harrabi, G. Fitch, D. G. Cory, Y. Nakamura, J.-S. Tsai, and W. D. Oliver, Noise spectroscopy through dynamical decoupling with a superconducting flux qubit, Nature Physics **7**, 565 (2011).

[36] B. Pokharel, N. Anand, B. Fortman, and D. A. Lidar, Demonstration of fidelity improvement using dynamical decoupling with superconducting qubits, Physical Review Letters **121**, 220502 (2018).

[37] J. F. Fitzsimons, Private quantum computation: an introduction to blind quantum computing and related protocols, npj Quantum Information **3**, 23 (2017).

[38] K. S. Chou, J. Z. Blumoff, C. S. Wang, P. C. Reinhold, C. J. Axline, Y. Y. Gao, L. Frunzio, M. H. Devoret, L. Jiang, and R. J. Schoelkopf, Deterministic teleportation of a quantum gate between two logical qubits, Nature **561**, 368 (2018).

[39] Y. Wan, D. Kienzler, S. D. Erickson, K. H. Mayer, T. R. Tan, J. J. Wu, H. M. Vasconcelos, S. Glancy, E. Knill, D. J. Wineland, A. C. Wilson, and D. Leibfried, Quantum gate teleportation between separated qubits in a trapped-ion processor, Science **364**, 875 (2019).

[40] H. Yan, Y. P. Zhong, H.-S. Chang, A. Bienfait, M.-H. Chou, C. R. Conner, É. Dumur, J. Grebel, R. G. Povey, and A. N. Cleland, Supplementary material, .

[41] E. Jeffrey, D. Sank, J. Mutus, T. White, J. Kelly, R. Barends, Y. Chen, Z. Chen, B. Chiaro, A. Dunsworth, A. Megrant, P. O'Malley, C. Neill, P. Roushan, A. Vainsencher, J. Wenner, A. Cleland, and J. M. Martinis, Fast accurate state measurement with superconducting qubits, Physical Review Letters **112**, 190504 (2014).

[42] C. Macklin, K. O'Brien, D. Hover, M. E. Schwartz, V. Bolkhovsky, X. Zhang, W. D. Oliver, and I. Siddiqi, A near-quantum-limited Josephson traveling-wave parametric amplifier, Science **350**, 307 (2015).

[43] K. Fujii and K. Yamamoto, Entanglement purification with double selection, Physical Review A **80**, 042308 (2009).

[44] S. Krastanov, V. V. Albert, and L. Jiang, Optimized entanglement purification, Quantum **3**, 123 (2019).

[45] J. Koch, T. M. Yu, J. Gambetta, A. A. Houck, D. I. Schuster, J. Majer, A. Blais, M. H. Devoret, S. M. Girvin, and R. J. Schoelkopf, Charge-insensitive qubit design derived from the cooper pair box, Physical Review A **76**, 042319 (2007).

[46] R. Barends, J. Kelly, A. Megrant, D. Sank, E. Jeffrey, Y. Chen, Y. Yin, B. Chiaro, J. Mutus, C. Neill, P. O'Malley, P. Roushan, J. Wenner, T. C. White, A. N. Cleland, and J. M. Martinis, Coherent Josephson qubit suitable for scalable quantum integrated circuits, Physical Review Letters **111**, 080502 (2013).

[47] Y. Chen, C. Neill, P. Roushan, N. Leung, M. Fang, R. Barends, J. Kelly, B. Campbell, Z. Chen, B. Chiaro, A. Dunsworth, E. Jeffrey, A. Megrant, J. Mutus, P. O'Malley, C. Quintana, D. Sank, A. Vainsencher, J. Wenner, T. White, M. R. Geller, A. Cleland, and J. M. Martinis, Qubit architecture with high coherence and fast tunable coupling, Physical Review Letters **113**, 220502 (2014).

[48] M. Steffen, M. Ansmann, R. C. Bialczak, N. Katz, E. Lucero, R. McDermott, M. Neeley, E. M. Weig, A. N. Cleland, and J. M. Martinis, Measurement of the entanglement of two superconducting qubits via state tomography, Science **313**, 1423 (2006).

[49] R. C. Bialczak, M. Ansmann, M. Hofheinz, E. Lucero, M. Neeley, A. D. O'Connell, D. Sank, H. Wang, J. Wenner, M. Steffen, A. N. Cleland, and J. M. Martinis, Quantum process tomography of a universal entangling gate implemented with Josephson phase qubits, Nature Physics **6**, 409 (2010).

[50] M. Reagor, W. Pfaff, C. Axline, R. W. Heeres, N. Ofek, K. Sliwa, E. Holland, C. Wang, J. Blumoff, K. Chou, M. J. Hatridge, L. Frunzio, M. H. Devoret, L. Jiang, and R. J. Schoelkopf, Quantum memory with millisecond coherence in circuit QED, Physical Review B **94**, 014506 (2016).

[51] A. P. M. Place, L. V. H. Rodgers, P. Mundada, B. M. Smitham, M. Fitzpatrick, Z. Leng, A. Premkumar, J. Bryon, A. Vrajitoarea, S. Sussman, G. Cheng, T. Madhavan, H. K. Babla, X. H. Le, Y. Gang, B. Jäck, A. Gyenis, N. Yao, R. J. Cava, N. P. de Leon, and A. A. Houck, New material platform for superconducting transmon qubits with coherence times exceeding 0.3 milliseconds, Nature Communications **12**, 1779 (2021).

[52] T. Yamamoto, M. Neeley, E. Lucero, R. C. Bialczak, J. Kelly, M. Lenander, M. Mariantoni, A. D. O'Connell, D. Sank, H. Wang, M. Weides, J. Wenner, Y. Yin, A. N. Cleland, and J. M. Martinis, Quantum process tomography of two-qubit controlled-Z and controlled-NOT gates using superconducting phase qubits, Physical Review B **82**, 184515 (2010).

[53] J. Qiu, Y. Zhou, C.-K. Hu, J. Yuan, L. Zhang, J. Chu, W. Huang, W. Liu, K. Luo, Z. Ni, X. Pan, Z. Yang, Y. Zhang, Y. Chen, X.-H. Deng, L. Hu, J. Li, J. Niu, Y. Xu, T. Yan, Y. Zhong, S. Liu, F. Yan, and D. Yu, Suppressing coherent two-qubit errors via dynamical decoupling (2021), arXiv:2104.02669.

[54] Z. Chen, K. J. Satzinger, J. Atalaya, A. N. Korotkov, A. Dunsworth, D. Sank, C. Quintana, M. McEwen, R. Barends, P. V. Klimov, S. Hong, C. Jones, A. Petukhov, D. Kafri, S. Demura, B. Burkett, C. Gidney, A. G. Fowler, A. Paler, H. Putterman, I. Aleiner, F. Arute, K. Arya, R. Babbush, J. C. Bardin, A. Bengtsson, A. Bourassa, M. Broughton, B. B. Buckley, D. A. Buell, N. Bushnell, B. Chiaro, R. Collins, W. Courtney, A. R. Derk, D. Eppens, C. Erickson, E. Farhi, B. Foxen, M. Giustina, A. Greene, J. A. Gross, M. P. Harrigan, S. D. Harrington, J. Hilton, A. Ho, T. Huang, W. J. Huggins, L. B. Ioffe, S. V. Isakov, E. Jeffrey, Z. Jiang, K. Kechedzhi, S. Kim, A. Kitaev, F. Kostritsa, D. Landhuis, P. Laptev, E. Lucero, O. Martin, J. R. McClean, T. McCourt, X. Mi, K. C. Miao, M. Mohseni, S. Montazeri,

W. Mruczkiewicz, J. Mutus, O. Naaman, M. Neeley, C. Neill, M. Newman, M. Y. Niu, T. E. O'Brien, A. Opremcak, E. Ostby, B. Pató, N. Redd, P. Roushan, N. C. Rubin, V. Shvarts, D. Strain, M. Szalay, M. D. Trevithick, B. Villalonga, T. White, Z. J. Yao, P. Yeh, J. Yoo, A. Zalcman, H. Neven, S. Boixo, V. Smelyanskiy, Y. Chen, A. Megrant, and J. Kelly, Exponential suppression of bit or phase errors with cyclic error correction, Nature **595**, 383 (2021).

[55] F. Motzoi, J. M. Gambetta, P. Rebentrost, and F. K. Wilhelm, Simple pulses for elimination of leakage in weakly nonlinear qubits, Physical Review Letters **103**, 110501 (2009).

[56] E. Knill, D. Leibfried, R. Reichle, J. Britton, R. B. Blakestad, J. D. Jost, C. Langer, R. Ozeri, S. Seidelin, and D. J. Wineland, Randomized benchmarking of quantum gates, Physical Review A **77**, 012307 (2008).

Supplementary Material for "Entanglement purification and protection in a superconducting quantum network"

I. DEVICE AND EXPERIMENTAL SETUP

The device and setup used in this experiment are identical to those used in Ref. [S1] except that the qubit operating points are different in this experiment. The simplified circuit diagram of the device is shown in Fig. S1. The center qubit $Q_2^{A,B}$ in each node is directly wire-bonded to the 1-m long superconducting NbTi coaxial cable with a tunable inductive coupler $G^{A,B}$ [S2]. The coupling strength $g^{A,B}$ is tuned with a dedicated flux line. More details on the fabrication and measurement system can be found in Ref. [S1]. The parameters of the qubits are listed in Section II.

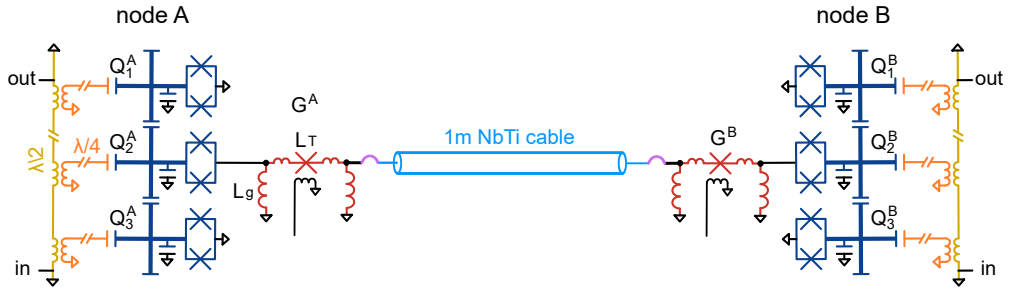

Figure S1. Circuit diagram for two-node network. More details can be found in Ref. [S1].

II. QUBIT AND CABLE CHARACTERIZATION

The basic qubit parameters are shown in Table S1. The inductance of the coupler G^k contributes to the total inductance of the qubit Q_2^k, which decreases Q_2^k's anharmonicity. T_ϕ is determined by a Ramsey measurement. As qubits Q_2^k operate near their maximum frequency points, these qubits have longer dephasing time than the other qubits $Q_{1,3}^k$. To achieve fast readout of qubits, we include a Purcell filter [S3] between the readout resonators and the readout line in each node. The Purcell filter has a resonant frequency of around 6.5 GHz, protecting the qubit from decay through the readout resonator. In node A, we use a traveling-wave parametric amplifier (TWPA) [S4] as the first-stage amplifier for the readout signal. The resulting average readout visibilities of the qubit $|g\rangle$ and $|e\rangle$ states are around 95%, limited by the qubit lifetime and residual excited-state

	$f_{eg}^{\max}$(GHz)	f_{eg}(GHz)	η(GHz)	$T_1(\mu s)$	$T_\phi(\mu s)$	f_{rr}(GHz)	τ_{rr}(ns)	F_g	F_e
Q_1^A	6.03	5.2556	-0.23	8.9	1.8	6.6050	350	0.968	0.940
Q_2^A	6.14	5.8695	-0.15	5.7	3.1	6.5497	450	0.974	0.927
Q_3^A	6.04	5.5055	-0.23	6.3	2.5	6.5032	300	0.962	0.926
Q_1^B	6.08	5.3021	-0.23	22.1	2.2	6.5056	400	0.988	0.936
Q_2^B	6.25	5.8901	-0.15	9.2	3.0	6.5560	600	0.965	0.939
Q_3^B	6.16	5.3218	-0.23	21.1	1.8	6.6080	350	0.983	0.939

Table S1. Qubit parameters. The maximum qubit frequency is $f_{eg}^{\max}$ and f_{eg} is the qubit operating frequency used here; η is the qubit anharmonicity; T_1 and T_ϕ are the qubit lifetime and pure dephasing time at the operating point; f_{rr} is the readout resonator frequency; τ_{rr} is the readout pulse duration; and F_g and F_e are the readout visibilities of $|g\rangle$ and $|e\rangle$ states, respectively.

population.

We use randomized benchmarking (RB) to characterize the single qubit gate performance [S5]. Our single-qubit π gate duration is 30 ns and $\pi/2$ gate duration is 20 ns, for all rotation axes, with gate durations optimized to balance qubit lifetime with state leakage. To minimize the effect of the second excited state $|f\rangle$, we use a DRAG correction for all our single qubit gates [S6]. We get an average single qubit RB gate fidelity of 99.8%.

We tune the frequency of our qubits to implement iSWAP and CZ gates. To swap an excitation between Q_1^k and Q_2^k in the same node, we bring Q_1^k and Q_2^k on resonance. At $\tau_{\mathrm{iSWAP}} = \pi/2g_{12}^k \approx 15$ ns ($k = A, B$), we complete the $|eg\rangle \rightarrow -i|ge\rangle$ process, which forms a iSWAP gate. To measure the efficiency of the iSWAP gate, we first rotate Q_2^k to $|e\rangle$ and measure the excited state population P_e. Next, with Q_2^k in $|g\rangle$, we prepare Q_1^k in $|e\rangle$, then swap the excitation to Q_2^k, followed by a measurement of P_e for Q_2^k. Comparing the resulting P_e in the two experiments, we find a swap efficiency of $\sim 99\%$.

To implement a CZ gate between Q_1^k and Q_2^k, we bring $|ee\rangle$ and $|gf\rangle$ on resonance. When $|ee\rangle$ is on resonance with $|gf\rangle$, the two-qubit state will evolve as $|ee\rangle \rightarrow -i|gf\rangle \rightarrow -|ee\rangle$, yielding a CZ gate in a time $\tau_{\mathrm{CZ}} \approx 21$ns. To characterize the gate performance, we perform process tomography [S7] to obtain the process χ matrix of the CZ gate. To overcome the issue of dynamical phase accumulated during the CZ gate, here we directly tune the phase of the tomography pulses to get the right CZ gate process χ matrix. We find process fidelities $\mathcal{F}_p = \mathrm{Tr}(\chi_{\mathrm{ideal}} \cdot \chi_{\mathrm{exp}})$ for the CZ

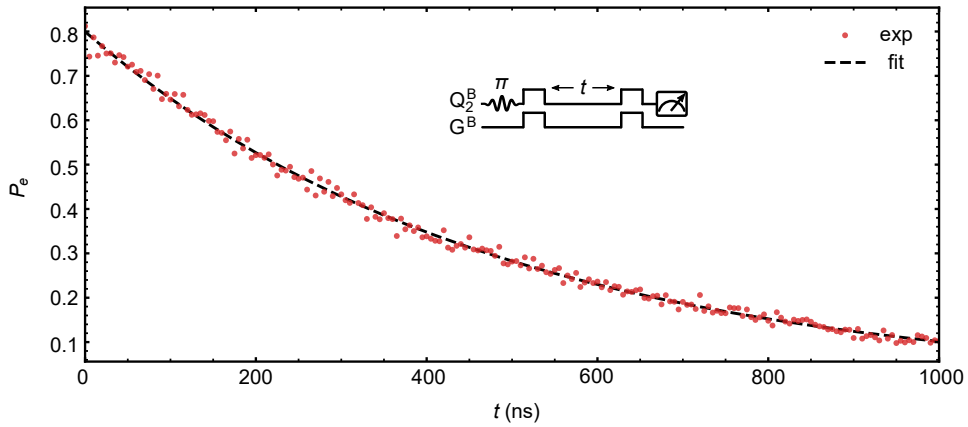

Figure S2. T_{1r} measurement of the 5.806 GHz cable mode. We prepare Q_2^B in $|e\rangle$ and swap the excitation to the cable mode, wait for a time delay t, then swap the excitation back to the qubit and measure the excited state population P_e. The swap duration is fixed to 30 ns. The measured T_{1r} is 477.3 ± 8.1 ns.

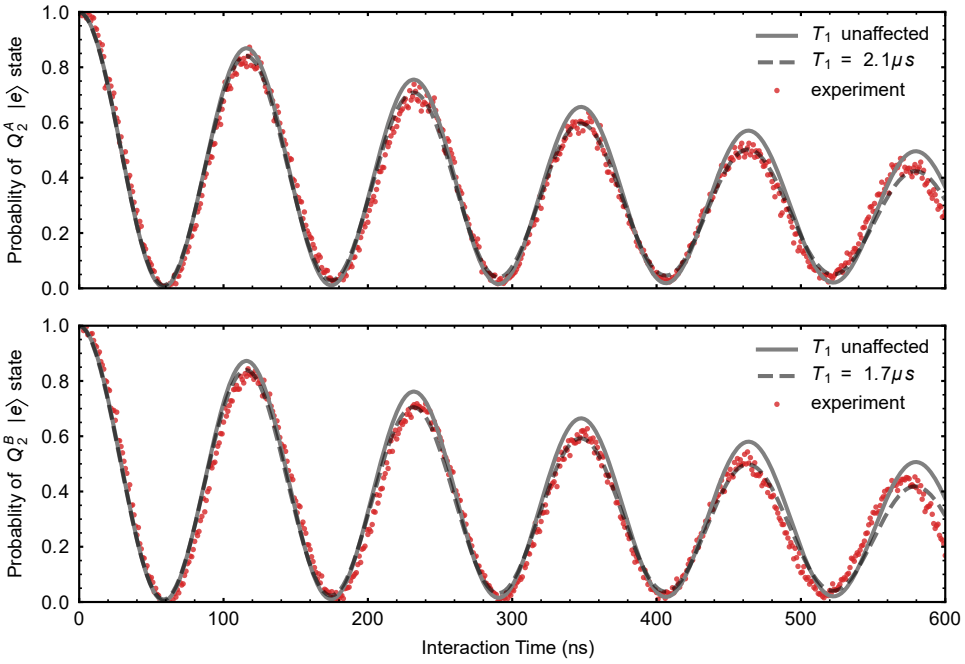

Figure S3. Vacuum Rabi oscillation between 5.806 GHz mode and Q_2^A (top panel) and Q_2^B (bottom panel). Red circles are experimental data, gray lines are numerical simulations with T_1 as shown in Table S1. Grey dashed lines are numerical simulations with shortened T_1, which implies that T_1 is affected by the coupling strength between the qubit and cable [S1].

gate between $Q_1^A - Q_2^A$ and $Q_1^B - Q_2^B$ of $95.93\% \pm 0.64\%$ and $95.05\% \pm 0.68\%$, respectively. With two $\pi/2$ single qubit gates and a CZ gate, we can implement a CNOT gate. To overcome the dynamical phase problem in experiment, we fix one $\pi/2$ gate phase and tune the phase of the other $\pi/2$ gate. The CNOT gate in the experiment will introduce additional phase differences between the two qubits, but this is unimportant for the purification experiment, where we only correct damping errors.

We use the center qubits Q_2^k to characterize the communication mode in the cable. Each qubit is coupled to the cable with a tunable inductive coupler G^k. The effective coupling strength g_n between the qubit and the nth Fabry-Pérot mode in the cable is given by [S8]

$$g_n = \frac{\sqrt{\omega_q \omega_n}}{2} \frac{M}{\sqrt{(L_J + L_g)(L_n + L_g)}}, \tag{S1}$$

where ω_q is the qubit frequency, ω_n is the nth mode frequency, L_J is the qubit inductance, L_n is inductance of the lumped element of the nth mode ($L_n \sim 121$ nH for the 5.806 GHz mode, with $n \approx 55$), and $L_g = 0.2$ nH is the inductance to ground (see Fig. S1). M is the effective mutual inductance between the qubit and the communication mode,

$$M = \frac{L_g^2}{2L_g + L_w + L_T/\cos\delta}, \tag{S2}$$

where δ is the flux-tunable phase across the coupler Josephson junction, $L_T \approx 0.62$ nH is the coupler inductance at $\delta = 0$, and $L_w \approx 0.1$ nH is the stray wiring inductance is series with L_T. The maximum coupling strength achieved by tuning δ is $g_{\max}/2\pi \approx 28$ MHz. The qubit frequency is slightly shifted when the coupling is turned on, which is compensated using a qubit Z pulse. Here we focus on the 5.806 GHz communication mode and only turn on the coupler during the Bell state generation. To characterize this mode, we first prepare Q_2^B in $|e\rangle$ and swap the excitation to the cable, leave the excitation in the cable mode for a time t and then swapping it back to Q_2^B to measure the remnant excitation, shown in Fig. S2. The swap duration used for this measurement is 30 ns. The measured T_{1r} is 477.3 ± 8.1 ns, corresponding to a quality factor $Q = 1.7 \times 10^4$. To characterize the performance when the coupler is turned on, we measure the vacuum Rabi oscillations between the cable mode and qubit, shown in Fig. S3. Numerical simulations show that the qubit T_1 and T_ϕ are shortened to around 2 μs and 1 μs respectively, likely due to losses associated with the wire-bond connection [S1].

III. STATE TOMOGRAPHY AND READOUT CORRECTION

The density matrices are characterized using quantum state tomography [S9], where we apply gates from the set $\{I, X/2, Y/2\}$ to each qubit after state generation, and perform simultaneous readout of all qubits. Density matrices are reconstructed from the nine measured probabilities and are constrained to be Hermitian and unitary.

To perform the process tomography [S7], we first prepare different initial states by applying gates from the set $\{I, X, X/2, Y/2\}$ to each qubit, perform the target process (i.e. CZ gate, state transfer) and do state tomography to determine the process χ matrix.

The single-shot measurements are repeated 8×10^3 times to extract probabilities. The measured probabilities $\mathbf{P^M} = (P_g^M, P_e^M)^T$ are corrected for readout errors using the pre-measured readout visibility data (F_g, F_e) [S10]. The state probabilities $\mathbf{P} = (P_g, P_e)^T$ are reconstructed by $\mathbf{P} = \mathbf{F}^{-1}\mathbf{P^M}$, where

$$\mathbf{F} = \begin{bmatrix} F_g & 1-F_e \\ 1-F_g & F_e \end{bmatrix}. \tag{S3}$$

Each measurement is repeated independently 20 times to estimate the overall uncertainties, defined as the standard deviation of these 20 measurements.

IV. NUMERICAL SIMULATIONS

The full Hamiltonian of our system in the rotating frame can be written using the following multi-qubit, multi-mode communication channel model:

$$\begin{aligned} H/\hbar = &\sum_{i=1,2,3}^{k=A,B} \Delta\omega_i^k \sigma_i^{k\dagger}\sigma_i^k + \sum_{m=1}^{M}\left(m - \frac{M+1}{2}\right)\omega_{\mathrm{FSR}} b_m^\dagger b_m \\ &+ \sum_{j=1,3}^{k=A,B} g_{j,2}^k(\sigma_2^k\sigma_j^{k\dagger} + \sigma_2^{k\dagger}\sigma_j^k) \\ &+ \sum_{m=1}^{M} g_m^A(\sigma_2^A b_m^\dagger + \sigma_2^{A\dagger} b_m) + \sum_{m=1}^{M}(-1)^m g_m^B(\sigma_2^B b_m^\dagger + \sigma_2^{B\dagger} b_m), \end{aligned} \tag{S4}$$

where σ_i^k and b_m are the annihilation operators for qubit Q_i^k and the mth cable mode respectively, $\Delta\omega_i^k$ is the qubit frequency detuning with respect to the rotating frame frequency, M is the number of standing modes considered in the simulation, ω_{FSR} is free spectral range of the cable modes, $g_{j,2}^k$ is the coupling strength between Q_j^k and Q_2^k, and g_m^k is the coupling strength between Q_2^k and

the mth cable mode. The rotating frame frequency is set to the frequency of the communication mode. The sign of g_m^B alternates with the mode number m due to the parity dependence of the standing wave modes.

In Fig. 1(b), only Q_2^A interacts with the communication mode, and is in resonance with that mode. The Hamiltonian can then be simplified to

$$H/\hbar = \sum_{m=1}^{M} \left(m - \frac{M+1}{2} \right) \omega_{\mathrm{FSR}} b_m^\dagger b_m + \sum_{m=1}^{M} g_m^A (\sigma_2^A b_m^\dagger + \sigma_2^{A\dagger} b_m) \tag{S5}$$

where we set $M = 3$ and constrain to a single excitation in the system. The master equation simulation is then compared to the experimental data, where the cable mode lifetime T_{1r} is as characterized in Fig. S2, but where we find that the qubit lifetime T_1 needs to be changed to $2.1\ \mu\mathrm{s}$ to better fit the experimental data (Fig. S3). We use the pure dephasing time T_ϕ shown in Table S1 in the simulations.

In Fig. 2(a-d), Q_1^k and Q_3^k are detuned away from Q_2^k. The time-dependent Hamiltonian can be simplified to

$$\begin{aligned} H(t)/\hbar = & \sum_{k=A,B} \Delta\omega_2^k(t) \sigma_2^{k\dagger} \sigma_2^k + \sum_{m=1}^{M} \left(m - \frac{M+1}{2} \right) \omega_{\mathrm{FSR}} b_m^\dagger b_m \\ & + \sum_{m=1}^{M} g_m^A(t) (\sigma_2^A b_m^\dagger + \sigma_2^{A\dagger} b_m) + \sum_{m=1}^{M} (-1)^m g_m^B(t) (\sigma_2^B b_m^\dagger + \sigma_2^{B\dagger} b_m) \end{aligned} \tag{S6}$$

where we set $M = 3$ and constrain to a single excitation in the system. We assume perfect rectangular pulses for the frequency changes and coupler modulations. The qubit lifetime T_1 is taken from fits to the vacuum Rabi oscillations (Fig. S3) when the coupler is on, and from Table S1 when the coupler is off; the pure dephasing time T_ϕ is from Table S1, and the cable mode lifetime is from Fig. S2.

In Fig. 3(c-g), the Bell states are simulated using Eq. S6, for which we assume perfect local operations. The first Bell pair decays during the second Bell pair generation, where we directly use Q_1^k's parameters in Table S1. In Fig. 4(c), the initial Bell state is also simulated using Eq. S6 above. We vary the qubit pure dephasing time T_ϕ and fix qubit T_1 to fit the simulations to the experimental data.

V. DISCUSSION OF ENTANGLEMENT PURIFICATION

The four Bell states $|\psi^{\pm}\rangle$, $|\phi^{\pm}\rangle$ are

$$|\psi^{\pm}\rangle = \frac{1}{\sqrt{2}}(|eg\rangle \pm |eg\rangle) \tag{S7}$$

$$|\phi^{\pm}\rangle = \frac{1}{\sqrt{2}}(|gg\rangle \pm |ee\rangle). \tag{S8}$$

The ideal Bell state via cable-mediated entanglement is $|\psi^{-}\rangle$,

$$\rho_{\text{ideal}} = |\psi^{-}\rangle\langle\psi^{-}| = \frac{1}{2}\begin{bmatrix} 0 & 0 & 0 & 0 \\ 0 & 1 & -1 & 0 \\ 0 & -1 & 1 & 0 \\ 0 & 0 & 0 & 0 \end{bmatrix}. \tag{S9}$$

For a bit-flip error channel with error probability p, the process is represented by the operators

$$E_0 = \sqrt{1-p}I, \tag{S10}$$

$$E_1 = \sqrt{p}X. \tag{S11}$$

If we assume only one qubit suffers from a bit-flip error, the final state will be

$$\rho = \sum_i I \otimes E_i \cdot \rho_{\text{ideal}} \cdot I \otimes E_i^{\dagger} = (1-\frac{p}{2})|\psi^{-}\rangle\langle\psi^{-}| + \frac{p}{2}|\phi^{-}\rangle\langle\phi^{-}|, \tag{S12}$$

with a fidelity $\mathcal{F} = 1 - p/2$. After applying the bit-purification circuit shown in Fig. S6(a), the final state fidelity will be

$$\mathcal{F}' = \frac{\mathcal{F}^2}{\mathcal{F}^2 + (1-\mathcal{F})^2}, \tag{S13}$$

with post-selection of $|gg\rangle$ or $|ee\rangle$.

For a phase-flip error channel, the process is represented by

$$E_0 = \sqrt{1-p}I, \tag{S14}$$

$$E_1 = \sqrt{p}Z. \tag{S15}$$

If we again assume only one qubit suffers from a phase-flip error, the final state will be

$$\rho = \sum_i I \otimes E_i \cdot \rho_{\text{ideal}} \cdot I \otimes E_i^{\dagger} = (1-\frac{p}{2})|\psi^{-}\rangle\langle\psi^{-}| + \frac{p}{2}|\psi^{+}\rangle\langle\psi^{+}|, \tag{S16}$$

with a final state fidelity $\mathcal{F} = 1 - p/2$, where $|\psi^{+}\rangle = (|eg\rangle + |ge\rangle)/\sqrt{2}$. The phase-purification circuit shown in in Fig. S6(**b**) acts in similar fashion to the bit-flip purification circuit.

Considering an amplitude-damping error channel, the channel representation is

$$E_0 = \begin{bmatrix} 1 & 0 \\ 0 & \sqrt{1-p} \end{bmatrix}, \tag{S17}$$

$$E_1 = \begin{bmatrix} 0 & \sqrt{p} \\ 0 & 0 \end{bmatrix}. \tag{S18}$$

Assuming only one qubit suffers an amplitude-damping error, the final state will be

$$\begin{aligned} \rho &= \sum_i I \otimes E_i \cdot \rho_{\text{ideal}} \cdot I \otimes E_i^\dagger \\ &= \frac{1+\sqrt{1-p}}{2}|\psi^-\rangle\langle\psi^-| + \frac{1-\sqrt{1-p}}{2}|\psi^+\rangle\langle\psi^+| + \frac{p}{2}(|gg\rangle\langle gg| - |ge\rangle\langle ge|) \\ &= \frac{1}{2}\begin{bmatrix} p & 0 & 0 & 0 \\ 0 & 1-p & -\sqrt{1-p} & 0 \\ 0 & -\sqrt{1-p} & 1 & 0 \\ 0 & 0 & 0 & 0 \end{bmatrix}, \end{aligned} \tag{S19}$$

with fidelity

$$\mathcal{F} = \frac{2-p+2\sqrt{1-p}}{4} \sim 1 - \frac{p}{2}. \tag{S20}$$

Applying the bit-purification circuit with post-selection of the $|gg\rangle$ state, the final state will be

$$\rho' = \frac{1}{2(1-p+p^2)}\begin{bmatrix} p^2 & 0 & 0 & 0 \\ 0 & (1-p)^2 & 1-p & 0 \\ 0 & 1-p & 1 & 0 \\ 0 & 0 & 0 & 0 \end{bmatrix}, \tag{S21}$$

$$\mathcal{F}' = \frac{(2-p)^2}{4(1-p+p^2)} \sim 1 - \frac{3p^2}{4}, \tag{S22}$$

With a success rate $(1-p+p^2)/2$ and only part of damping errors are corrected. If we do the post-selection with the $|ee\rangle$ state, the final state will be

$$\rho' = |\psi^+\rangle\langle\psi^+|, \tag{S23}$$

$$\mathcal{F}' = 1, \tag{S24}$$

with a success rate of $(1-p)/2$ and correcting all the damping errors.

If we consider both phase and amplitude-damping errors, the state before purification can be written as

$$\rho = (1-\epsilon_p)|\psi^-\rangle\langle\psi^-| + \epsilon_p|\psi^+\rangle\langle\psi^+| + \epsilon_d(|gg\rangle\langle gg| - |ge\rangle\langle ge|), \tag{S25}$$

$$\mathcal{F} = 1 - \frac{\epsilon_d}{2} - \epsilon_p. \tag{S26}$$

After applying the bit-purification circuit with post-selection of $|gg\rangle$, the final state will be

$$\rho' = \frac{1}{2(1-2\epsilon_d+4\epsilon_d^2)} \begin{bmatrix} 4\epsilon_d^2 & 0 & 0 & 0 \\ 0 & (1-2\epsilon_d)^2 & (1-2\epsilon_p)^2 & 0 \\ 0 & (1-2\epsilon_p)^2 & 1 & 0 \\ 0 & 0 & 0 & 0 \end{bmatrix}, \tag{S27}$$

$$\mathcal{F}' = \frac{1-\epsilon_d-2\epsilon_p+\epsilon_d^2+2\epsilon_p^2}{1-2\epsilon_d+4\epsilon_d^2} \tag{S28}$$

with a success rate $0.5-\epsilon_d+2\epsilon_d^2$ and non-zero ground state population $2\epsilon_d^2/(1-2\epsilon_d+4\epsilon_d^2)$. If we do the post-selection of $|ee\rangle$, the final state will be

$$\rho' = (1-\epsilon_p')|\psi^+\rangle\langle\psi^+| + \epsilon_p'|\psi^-\rangle\langle\psi^-|, \tag{S29}$$

$$\epsilon_p' = \frac{2\epsilon_p - 2\epsilon_p^2 - \epsilon_d}{1-2\epsilon_d}, \tag{S30}$$

$$\mathcal{F}' = 1-\epsilon_p' \cong 1+\epsilon_d-2\epsilon_p, \tag{S31}$$

with a success rate $0.5-\epsilon_d$ and zero ground state population.

To realize entanglement purification, we need to prepare at least two Bell pairs. Since there is only one channel in our system, this is done sequentially, first creating and then storing the first Bell pair in the storage qubits Q_1^k. In the experiment, we find that the Bell state fidelity suffers if we leave the qubit frequency of Q_1^A fixed (see Fig. S4). This could be due to two-photon processes between Q_1^A and Q_2^A during the excitation pulse used for generating the second Bell state, as when generating the second Bell pair, both Q_1^A and Q_2^A have a population in their $|e\rangle$ states. We find that when we tune Q_1^A's $|g\rangle - |e\rangle$ frequency from 5.25 GHz to ~ 4.9 GHz, the fidelity of the second Bell state is closer to that of the initial state fidelity.

For entanglement purification, we perform full state tomography of all the final states (Fig. S5). As is discussed in the main text, when the measurement results for $|Q_1^AQ_1^B\rangle$ are not consistent, the final state of $|Q_2^AQ_2^B\rangle$ will be a mixed state. When $|Q_1^AQ_1^B\rangle = |gg\rangle$, the final state of $|Q_2^AQ_2^B\rangle$

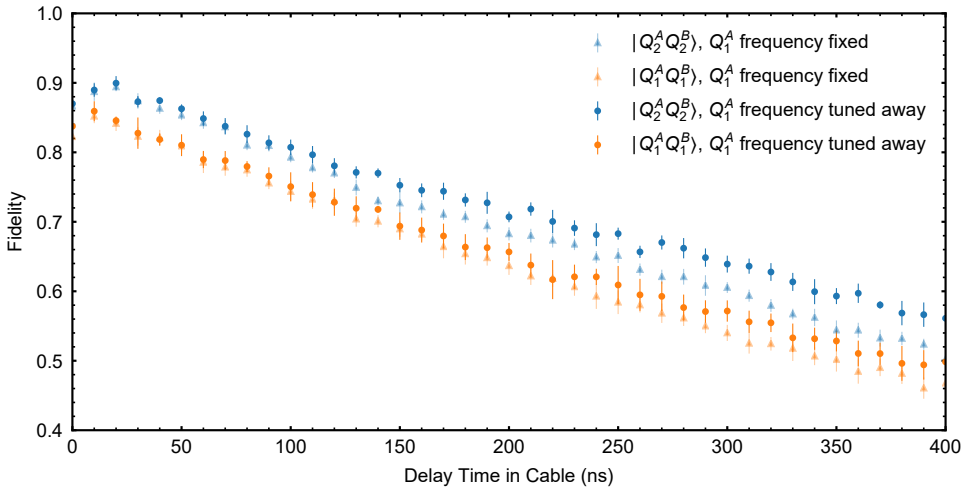

Figure S4. Bell state fidelity before purification with (circles) and without (triangles) tuning away Q_1^A's operating frequency. The fidelity decreases if Q_1^A's frequency is left fixed.

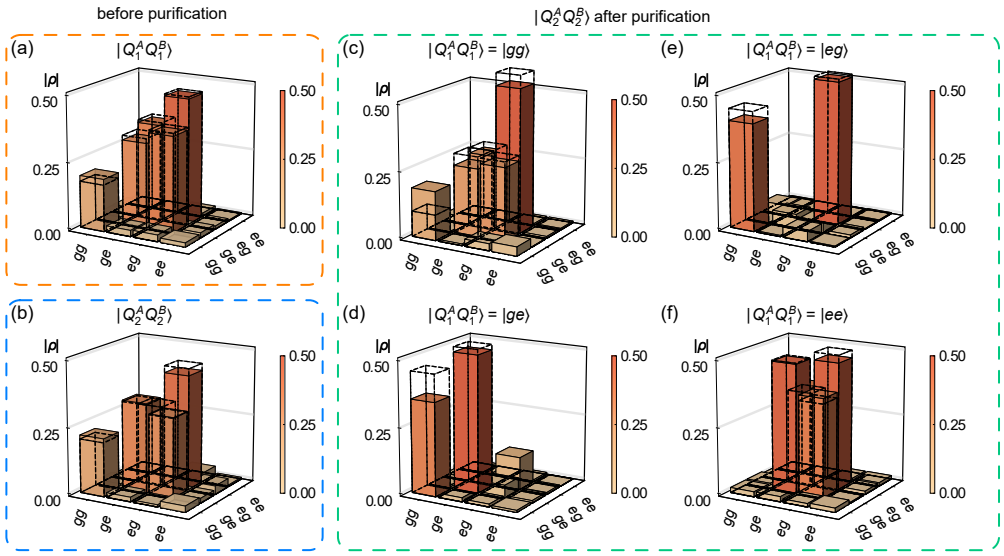

Figure S5. Full state tomography of entanglement purification results when $t_d = 150$ ns. (a-b) State tomography of (a) $|Q_1^A Q_1^B\rangle$ and (b) $|Q_2^A Q_2^B\rangle$ before purification. (c-f) State tomography of $|Q_2^A Q_2^B\rangle$ for different $|Q_1^A Q_1^B\rangle$ measurement results. Dashed lines are numerical simulation results.

will have both damping and phase errors. Only when $|Q_1^A Q_1^B\rangle = |ee\rangle$, then the damping error is corrected, consistent with the experimental measurements.

There are a number of other entanglement purification protocols [S11–S13] which can be implemented using this system. We performed numerical simulations to explore the expected results

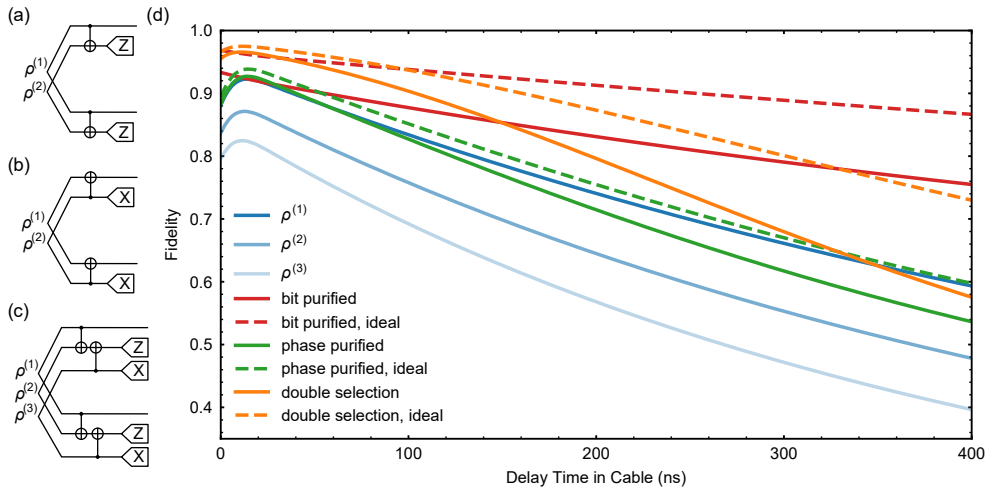

Figure S6. Results of numerical simulations to evaluate different entanglement purification protocols. (a-c) Different entanglement purification circuits used in numerical simulations: (a) bit-error purification circuit, (b) phase-error purification circuit, (c) double-selection purification circuit [S11]. (d) Simulated purification results for the protocols in (a-c). Blue lines are states before purification including (lightest) and not including (darkest) state decay during state storage. Simulated results are for the bit-purification (red), phase-purification (green) and purification with double selection (orange). Dashed lines are purification results with ideal Bell pairs $\rho^{(0)}$, while solid lines include state decay during storage.

of each protocol shown in Fig. S6. The bit-purification circuit has the best outcomes. When using the phase error correction circuit, there is negligible improvement after purification, which is as expected, as the main errors are due to amplitude damping. In the simulations, double-selection purification introduced in Ref. [S11] has similar performance to bit-purification when the cable delay t_d is small, but becomes worse when t_d is large, resulting in larger (and therefore dominant) amplitude damping errors. Here we only perform purification that corrects damping errors, as this has the best simulated performance. More complex purification protocols [S14] could be explored if we had a better quantum memory (e.g. larger T_1 in the storage qubits), or if we had multiple communication channels, avoiding the need to store the first Bell pair.

VI. DISCUSSION OF ENTANGLEMENT PROTECTION WITH DYNAMICAL DECOUPLING

In Fig. S7 we plot the performance of the dynamical decoupling method for different DD durations and Rabi drive strengths. We change the interval between each X gate in the DD sequence;

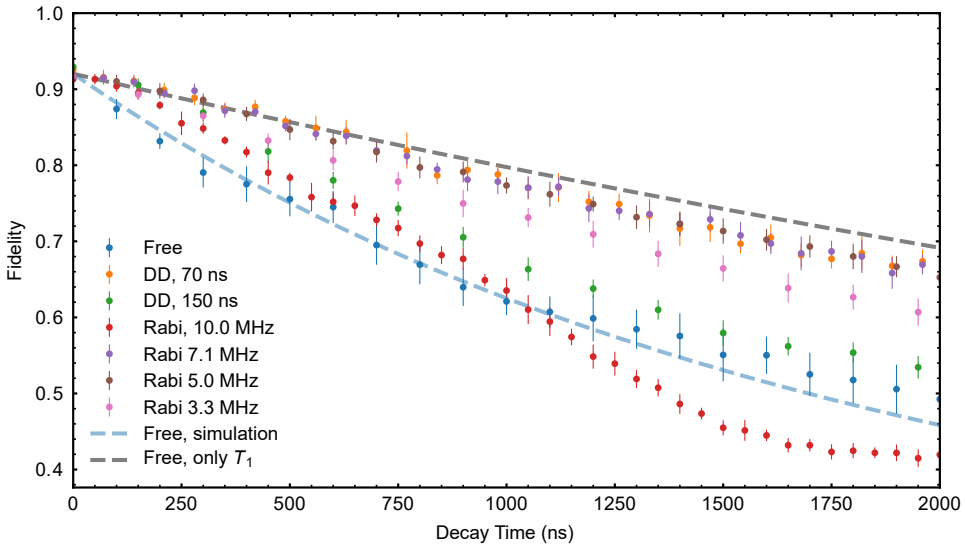

Figure S7. Bell state fidelity when varying the DD duration and Rabi drive strength.

the DD duration is the period for two complete X gates. We find that for longer DD durations, the fidelity decays faster. We also vary the Rabi drive strength, where we find that for a larger drive strength $\Omega/2\pi = 10.0$ MHz, the state fidelity decays much faster, which could be due to leakage to the higher excited states resulting in imperfect control of the qubit. For $\Omega/2\pi = 7.1$ MHz, the performance is similar to the value $\Omega/2\pi = 5.0$ MHz used in the main text.

We also tried to combine RD/DD with entanglement purification to improve the performance of purification. However, we found in the experiment that to preserve the fidelity of the first Bell pair in $|Q_1^A Q_1^B\rangle$ during the generation of the second Bell pair, it is necessary to frequency-bias Q_1^A away from Q_2^A (see Fig. S4). This frequency bias requires that we apply a z pulse to Q_1^A. We found experimentally that the DD/RD signals did not improve the Bell state fidelities when combined with the z pulses. It could due to spurious noise introduced by the z pulses, and/or imperfections in the pulse shapes. This meant we could not successfully combine DD/RD with purification.

[S1] Y. Zhong, H.-S. Chang, A. Bienfait, É. Dumur, M.-H. Chou, C. R. Conner, J. Grebel, R. G. Povey, H. Yan, D. I. Schuster, and A. N. Cleland, Deterministic multi-qubit entanglement in a quantum network, Nature **590**, 571 (2021).

[S2] Y. Chen, C. Neill, P. Roushan, N. Leung, M. Fang, R. Barends, J. Kelly, B. Campbell, Z. Chen, B. Chiaro, A. Dunsworth, E. Jeffrey, A. Megrant, J. Mutus, P. O'Malley, C. Quintana, D. Sank, A. Vainsencher, J. Wenner, T. White, M. R. Geller, A. Cleland, and J. M. Martinis, Qubit architecture with high coherence and fast tunable coupling, Physical Review Letters **113**, 220502 (2014).

[S3] E. Jeffrey, D. Sank, J. Mutus, T. White, J. Kelly, R. Barends, Y. Chen, Z. Chen, B. Chiaro, A. Dunsworth, A. Megrant, P. O'Malley, C. Neill, P. Roushan, A. Vainsencher, J. Wenner, A. Cleland, and J. M. Martinis, Fast accurate state measurement with superconducting qubits, Physical Review Letters **112**, 190504 (2014).

[S4] C. Macklin, K. O'Brien, D. Hover, M. E. Schwartz, V. Bolkhovsky, X. Zhang, W. D. Oliver, and I. Siddiqi, A near-quantum-limited Josephson traveling-wave parametric amplifier, Science **350**, 307 (2015).

[S5] E. Knill, D. Leibfried, R. Reichle, J. Britton, R. B. Blakestad, J. D. Jost, C. Langer, R. Ozeri, S. Seidelin, and D. J. Wineland, Randomized benchmarking of quantum gates, Physical Review A **77**, 012307 (2008).

[S6] F. Motzoi, J. M. Gambetta, P. Rebentrost, and F. K. Wilhelm, Simple pulses for elimination of leakage in weakly nonlinear qubits, Physical Review Letters **103**, 110501 (2009).

[S7] T. Yamamoto, M. Neeley, E. Lucero, R. C. Bialczak, J. Kelly, M. Lenander, M. Mariantoni, A. D. O'Connell, D. Sank, H. Wang, M. Weides, J. Wenner, Y. Yin, A. N. Cleland, and J. M. Martinis, Quantum process tomography of two-qubit controlled-Z and controlled-NOT gates using superconducting phase qubits, Physical Review B **82**, 184515 (2010).

[S8] Y. P. Zhong, H.-S. Chang, K. J. Satzinger, M.-H. Chou, A. Bienfait, C. R. Conner, É. Dumur, J. Grebel, G. A. Peairs, R. G. Povey, D. I. Schuster, and A. N. Cleland, Violating bell's inequality with remotely connected superconducting qubits, Nature Physics **15**, 741 (2019).

[S9] M. Steffen, M. Ansmann, R. C. Bialczak, N. Katz, E. Lucero, R. McDermott, M. Neeley, E. M. Weig, A. N. Cleland, and J. M. Martinis, Measurement of the entanglement of two superconducting qubits via state tomography, Science **313**, 1423 (2006).

[S10] R. C. Bialczak, M. Ansmann, M. Hofheinz, E. Lucero, M. Neeley, A. D. O'Connell, D. Sank, H. Wang, J. Wenner, M. Steffen, A. N. Cleland, and J. M. Martinis, Quantum process tomography of a universal entangling gate implemented with Josephson phase qubits, Nature Physics **6**, 409 (2010).

[S11] K. Fujii and K. Yamamoto, Entanglement purification with double selection, Physical Review A **80**, 042308 (2009).

[S12] C. H. Bennett, G. Brassard, S. Popescu, B. Schumacher, J. A. Smolin, and W. K. Wootters, Purification of noisy entanglement and faithful teleportation via noisy channels, Physical Review Letters **76**, 722 (1996).

[S13] L. Jiang, J. M. Taylor, A. S. Sørensen, and M. D. Lukin, Distributed quantum computation based on small quantum registers, Physical Review A **76**, 062323 (2007).

[S14] S. Krastanov, V. V. Albert, and L. Jiang, Optimized entanglement purification, Quantum **3**, 123 (2019).